fractal and fractional

MDPI

Article

Comparative Studies of Nonlinear Models and Their Applications to Magmatic Evolution and Crustal Growth of the Huai'an Terrane in the North China Craton

Qiuming Cheng [1,2,*] and Min Gao [3]

[1] State Key Lab of Geological Processes and Mineral Resources, China University of Geosciences (Beijing), Beijing 100083, China
[2] Frontier Science Center of Deep-Time Digital Earth, China University of Geosciences (Beijing), Beijing 100083, China
[3] Petroleum Exploration and Production Research Institute, SINOPEC, Beijing 100083, China; gm2020.syky@sinopec.com
* Correspondence: qiuming.cheng@iugs.org

Abstract: Power-law, inverse exponential and logarithmic models are widely used as empirical tools to describe anomalies in spatial and temporal geodynamic processes. However, the lack of clear interpretation of the relationships and distinctions among these models often makes their selection challenging, leaving them as empirical tools to be validated by data. This paper introduces these nonlinear functions derived from a unified differential equation, with parameters that reflect their relative nonlinearities and singularities, enabling their comparative application. By applying these functions to analyze magmatic events of the Huai'an Terrane, this study reveals two major crustal growth and reworking events between 2.6 and 1.7 Ga, each exhibiting distinctive nonlinear characteristics. The power-law function highlights strong nonlinearity and singularity during phases of intense magmatic activity, while logarithmic and exponential functions effectively characterize transitions between different tectonic processes. Geochemical data, including U-Pb zircon dating and Lu-Hf isotopic analyses, further validate the models by delineating distinct phases of crustal growth and reworking within the Trans-North China Orogen. The findings help connect the anomalies of frequency of magmatic events with the tectonic processes, providing important insights into the evolution processes of the North China Craton.

Keywords: magmatic events; nonlinearity; singularity; North China Craton; crustal growth; crustal reworking

Academic Editor: Zine El Abiddine Fellah

Received: 4 December 2024
Revised: 4 January 2025
Accepted: 9 January 2025
Published: 14 January 2025

Citation: Cheng, Q.; Gao, M. Comparative Studies of Nonlinear Models and Their Applications to Magmatic Evolution and Crustal Growth of the Huai'an Terrane in the North China Craton. *Fractal Fract.* **2025**, *9*, 38. https://doi.org/10.3390/fractalfract9010038

1. Introduction

In geoscience, anomalies can arise in various forms, such as unusual temperature patterns, flare-up magmatic activities, or seismic activities. Nonlinear processes of Earth systems, like tectonic plate interactions, volcanic activity and magmatic processes, contribute to these anomalies. Understanding these geology anomaly events is essential because they can reveal key insights into Earth's dynamic processes, such as mantle convection, crustal deformation and the effects of plate subduction or collisions. Whether linked to tectonic movements, volcanic activity or subsurface composition, anomalies caused by nonlinear processes provide valuable insights that drive scientific discovery. The concept of local singularity, grounded in multifractal theory and fractal derivative theory, offers a powerful framework to describe the nonlinear properties of extreme geological events and associated anomalies [1]. Singularity in geological processes arises when small changes or inputs

trigger disproportionately large effects, often due to nonlinear dynamics. Key mechanisms that cause such singularity in the Earth system include but are not limited to Multiplicative Cascade Processes (MCPs), Phase Transitions (PTs) and Self-Organized Criticality (SOC). MCPs such as diffusion, convection and turbulent flow in fluids or magma create feedback loops that amplify localized anomalies [2]. PTs involve change in state (e.g., solid–liquid–gas) that introduce sharp gradients and abrupt system changes. SOC includes systems like fault networks or sedimentary layers that evolve toward critical states, where minor triggers cause large-scale events. These anomalies are challenging to characterize through traditional statistical models due to their irregular, scale-dependent behavior and tendency for abrupt intensity changes across scales. Nonlinear models are essential for accurately capturing the inherent nonlinear patterns in these anomalies. This perspective enables a deeper understanding of the spatial and temporal complexities of extreme geological events, offering valuable insights into their behavior, prediction and management.

Indeed, one of the important properties of anomalies, especially in the context of geoscience, is the decay rate or pattern that describes how the anomaly diminishes or changes from the center toward the edge. This decay pattern often reveals key information about the underlying processes and mechanisms driving the anomaly. Understanding how an anomaly decays is crucial in interpreting its significance and potential impact. Several models or functions have been utilized to describe the decay regulations of anomalies. These include linear, logarithmic, exponential and power-law functions. However, the lack of clear interpretation of the relationships and distinctions among these models often makes their selection challenging, leaving them as empirical tools to be validated by data [3–5]. This gap can make it difficult for practitioners to understand how these functions are related and how they might be chosen for real-world scenarios and often based on validation of the datasets [6–8]. For example, it was stated in [8] that the power-law model remains one of the best-performing models, and other models that performed equally as well included the log-linear functional form in modeling concentration and discharge relations in hydrological modeling. The current paper demonstrates the derivation of these functions from a unified first-order differential equation, with parameters that highlight their distinct characteristics, including nonlinearity and singularity. Practical examples are provided to illustrate their applications to geological processes, with a focus on extreme magmatic events.

Different nonlinear functions such as inverse exponential, logarithmic and power-law models are applied to model the varying intensity and frequency of the magmatic events in the Huai'an terrane. Previous studies of tonalite–trondhjemite–granodiorite (TTG) gneisses and granites in the Huai'an terrane through U-Pb zircon dating, Lu-Hf isotopes and whole-rock geochemistry reveals a complex tectonic evolution, including periods of crustal growth (2.6–2.2 Ga), transition to crustal reworking (2.2–1.9 Ga) and crustal reformation (1.9–1.7 Ga) [9]. In the current paper, we demonstrate that in these phases, different nonlinear functions can be used to model the varying intensity and frequency of magmatic events. The results show that a power-law function can characterize the strong magmatic activity between 2.6 and 2.2 Ga, indicating a scaling relationship between event frequency density around a peak and time interval, with a distinct singularity. Logarithmic functions and exponential functions are used to analyze the transition phases where magmatic activity evolves from crustal growth to reworking, reflecting a gradual shift in the tectonic conditions. These models help connect the anomalies of frequency of magmatic events with the tectonic processes, providing important insights into the formation and evolution processes of the North China Craton (NCC).

2. Methods

In the context of nonlinear dynamics and fractal calculus, the density of an attribute within a dynamic system can be studied as a temporal process, with density variations over time. For an attribute with density $\rho(t)$ at time t, this density is the result of underlying dynamic processes acting over time and can be modeled as $< \rho(t) >$, which represents the expected density of the attribute at any given moment.

In a simple, linear temporal system where changes in density are solely due to uniform decay over time, we might assume a first-order decay model where the rate of change of $< \rho(t) >$ with respect to time t is proportional to the density itself with a constant decay rate λ [10]:

$$\frac{d < \rho(t) >}{dt} = -\lambda < \rho(t) > . \tag{1}$$

Solving the above equation yields the following exponential decay model:

$$< \rho(t) >= ce^{-\lambda t}. \tag{2}$$

This solution indicates that in a homogeneous, uniform system, attribute density decreases exponentially over time. Here, the system is smooth and linear, meaning that higher-order derivatives of $< \rho(t) >$ will remain proportional to the original function, such that each derivative simply scales the density by $(-\lambda)^n$, where n is the order of the derivatives. This temporal model is commonly observed in systems with uniform decay, such as radioactive decay in rocks or gravitationally driven water flow in a simple drainage network [11].

However, when considering systems in heterogeneous media or influenced by complex cascade processes over time—such as intermittent convective pulses, variable diffusion rates, or cyclic fluxes—the decay behavior deviates from uniformity. In these cases, the temporal change rate λ itself may fluctuate, influenced by irregular or nonstationary processes that lead to faster or slower decay rates. For example, the change rate of density is proportional to the density itself $< \rho(t) >$ with a variable decay rate (–λ(t)) that changes with a change in scale (t) [12].

$$\frac{d < \rho(t) >}{dt} = -\frac{1}{\lambda(t)} < \rho(t) >^{\gamma}, \tag{3}$$

where λ(t) is the coefficient as a function of scale t and γ is an integer index of nonlinearity. To solve Equation (3), one needs to know the functional form of λ(t). It is usually not possible to know the exact expression of this function since it may have different forms depending on the complexity of the system. However, the coefficient function $1/\lambda(t)$ can be approximated using the Taylor series expansion of $1/[\lambda(1/t)]$ as follows [12]:

$$\frac{1}{\lambda(t)} = \lambda_0 + \lambda_1 \frac{1}{t} + \lambda_2 \frac{1}{t^2} + o(\frac{1}{t^2}), \tag{4}$$

where the components λ_0, λ_1 and λ_2 correspond to the coefficients of the first three orders of $1/t$. The remainder term states that the error for the approximation approaches zero when t decreases to zero and the order of the error is smaller than the order of $(1/t^2)$. Using this approximation, one can express the differential model as follows:

$$\frac{d < \rho(t) >}{dt} \approx -(\lambda_0 + \lambda_1 \frac{1}{t} + \lambda_2 \frac{1}{t^2}) < \rho(t) >^{\gamma} . \tag{5}$$

Further simplifying the model by setting $\gamma = 1$, the new model (5) represents the combination of three different types of forms: normal exponential, power-law and exponential of inverse time:

$$< \rho(t) >= ct^{-\lambda_1} e^{-\lambda_0 t + \lambda_2 \frac{1}{t}}. \quad (6)$$

Model (6) gives a new four-parameter model with the parameter c as constant and λ_0, λ_1 and λ_2 representing the coefficients of the first three increment terms, respectively. In model (6), both the first term, $e^{-\lambda_0 t}$, and the third term, $e^{\lambda_2 \frac{1}{t}}$, are monotonically decreasing exponential functions of t, whereas the second term $t^{-\lambda_1}$ represents the monotonically decreasing power-law function of t. This new model can be converted into a simple form by applying logarithmic transformation to both sides of (6):

$$Log\rho(t) \; = \; c - \lambda_0 t - \lambda_1 Log(t) + \lambda_2 t^{-1}. \quad (7)$$

The above model indicates that a general system can be approximated by combining the three models with four parameters. The first exponential model characterizes the non-singular decay rate, whereas the other two models characterize the singular decay rate.

If we set $\gamma = 0$, the solution of model (5) results in a combination of three different forms: linear, logarithmic and inverse time:

$$< \rho(t) >= c - \lambda_0 t - \lambda_1 Log(t) - \lambda_2 t^{-1}. \quad (8)$$

The primary difference between model (8) and model (7) lies in the logarithmic transformation of the density in model (7). These two solution forms, (7) and (8), indicate that the forms in solution (7) generally exhibit higher nonlinearity compared to those in solution (8). By comparing all six types of functions involved in solutions (7) and (8), the functions can be ranked by their degree of nonlinearity, from the weakest to strongest: linear, logarithmic, inverse time, exponential, power-law and exponential with inverse time.

When analyzing both the singularity and nonlinearity of the six functions as $t \to 0$, we can combine their behaviors into a comprehensive framework. The details of nonlinearity and singularity of these functions are summarized in Table 1.

Table 1. Nonlinearity and singularity analysis of functions as $t \to 0$.

Function	Form of the Function	Singularity	Nonlinearity	Combined Behavior
Linear Function	f(t) = t	Non-singular	None	Smooth, finite and entirely predictable.
Logarithmic Function	f(t) = log(t)	Weakly singular	Weak	Exhibits mild nonlinearity with weak singularity.
Inverse Time Function	f(t) = 1/t	Strongly singular	Moderate	A strongly singular and moderately nonlinear function.
Exponential Function	f(t) = exp($-\lambda_0$t)	Non-singular	Moderate	A non-singular function with moderate nonlinearity.
Power-law Function	$f(t) = t^{-\lambda_1}$	Moderately singular	Strong	A strongly nonlinear and moderately singular function.
Exponential with Inverse Time Function	f(t) = exp(λ_2/t)	Strong singularity	Very strong	A strong singular and highly nonlinear function.

Linear functions are the most straightforward, with no singularity or nonlinearity. Logarithmic functions diverge weakly and are only slightly nonlinear. Inverse time functions (special case of power-law function with -1 as exponent) exhibit both strong singularity and moderate nonlinearity, making them more sensitive near $t = 0$. Exponential functions are non-singular but moderately nonlinear, offering a smooth and finite decay. Power-law functions are strongly nonlinear and moderately singular, with divergence strength controlled by λ_1. Exponential with inverse time functions are strongly singular and exhibit strong nonlinearity, combining rapid decay with sensitivity near $t = 0$. Figure 1 illustrates the curves of the linear, logarithmic, exponential and power-law functions fitted to a same dataset for visualization purpose.

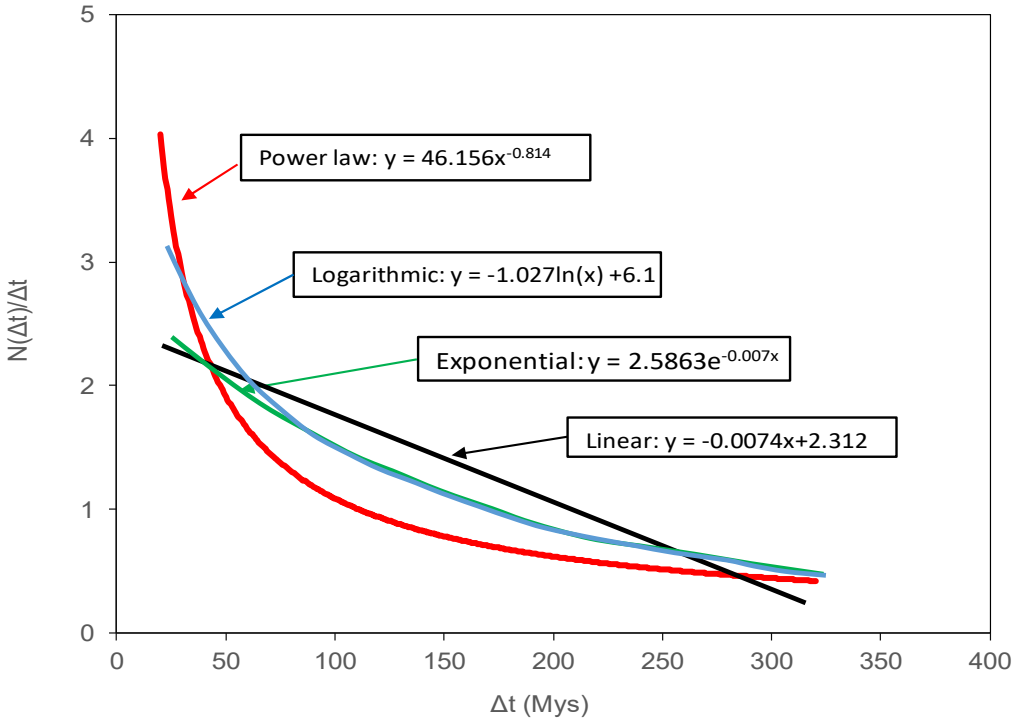

Figure 1. Illustration of curves drawn based on four types of functions: linear, logarithmic, exponential and power-law. These functions were fitted to a dataset using least squares (LS) for visualization purposes.

This combined analysis reveals the interplay between singularity and nonlinearity, with some functions (e.g., power-law) showing both strong properties, while others (e.g., exponential) balance nonlinearity with smoothness. Model (6) can be used as a combined model as used in [12] for describing the frequency of floods in the Great Toronto Area, in [13] for describing the frequency distribution of the grade of porphyry copper deposits of the world, and in [14] for describing geochemical anomalies in a vertical profile in a mineral district in Inner Mongolia. The combined model of power-law and power-law with exponential cutoff was also applied in [4] for biodiversity estimation and turning-point prediction for Coronavirus Diease-2019 (COVID-19) infection/fatality. One property that distinguishes the power-law model from other functions is its scale-invariance or self-similarity, which is commonly associated with fractal systems [15,16]. To model irregularities around a location or time point with a singularity in density, we turn to fractal or fractional calculus, where derivatives are defined at non-integer orders. For further discussion on fractal density and fractal calculus, refer to [17].

3. Magmatic Activities Concerning Tectonic Evolution

The NCC, one of the oldest cratons on the globe, is composed of the Eastern Block, the Western Block and the Trans-North China Orogen (TNCO) [18]. The Western Block comprises the Yinshan Block, Orodos Block and the Khondalite Belt. The TNCO is further subdivided into seven metamorphic terranes from north to south: Chengde, North Hebei, Xuanhua, Huai'an, Hengshan, Wutai, Fuping, Lüliang, Zanhuang, Zhongtiao, Dengfeng and Taihua terranes [18] (Figure 2). The study area selected for this research is the Huai'an terrane, situated on the northwestern edge of the TNCO, at the conjunction of the TNCO and the Khondalite Belt of the Western Block in the NCC (Figure 2). The Huai'an terrane has undergone complex tectonic evolution and intense magmatic activity during the Paleoproterozoic, making it an important window for understanding the tectonic processes of the NCC [19–21].

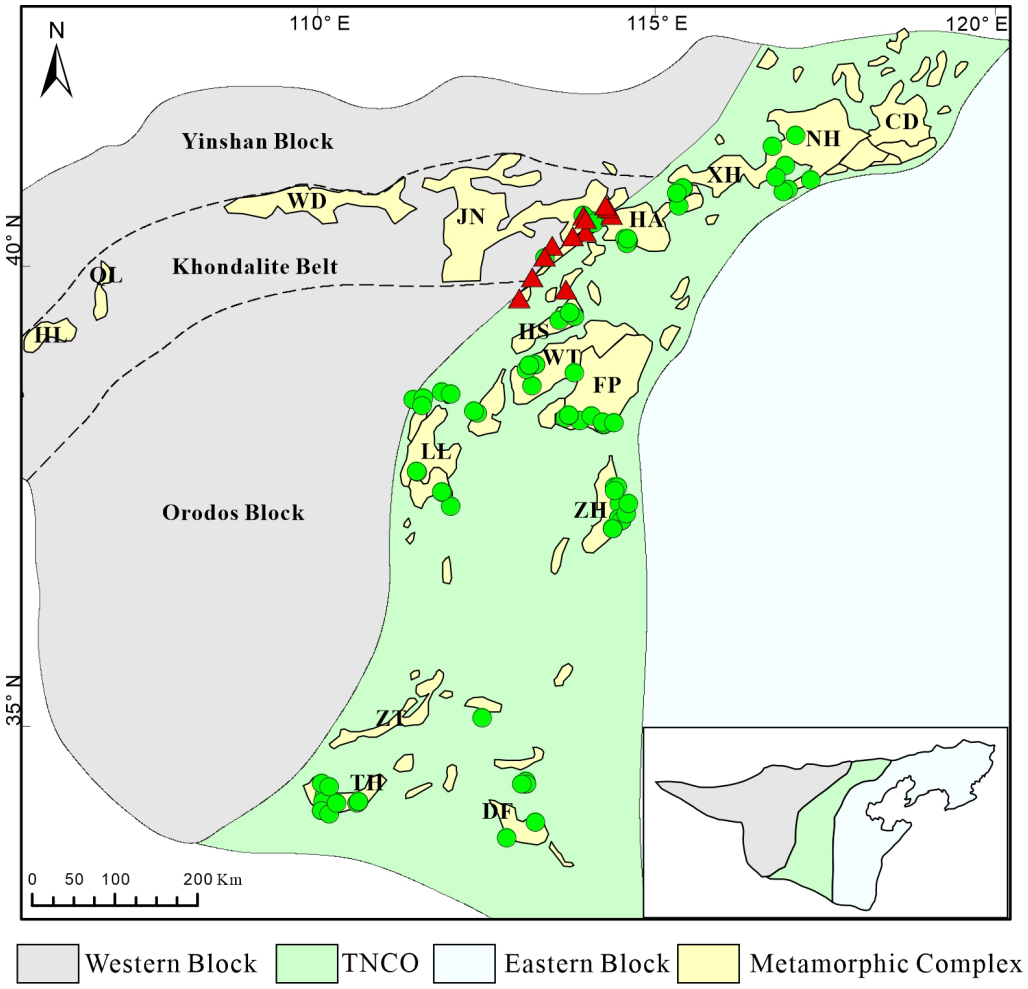

Figure 2. Granite sample locations in the TNCO of the NCC. The insert shows the geological framework of the NCC (after [18]). Triangles and dots represent granite samples from this paper and published papers, respectively. Abbreviations for metamorphic complexes: Chengde (CD), North Hebei (NH), Xuanhua (XH), Huai'an (HA), Hengshan (HS), Wutai (WT), Fuping (FP), Lüliang (LL), Zanhuang (ZH), Zhongtiao (ZT), Taihua (TH), Dengfeng (DF), Jining (JN), Wulashan-Daqingshan (WD), Qianlishan (QL), and Helanshan (HL).

The tectonic evolution of the NCC during the Paleoproterozoic can be divided into two primary phases of activity. In the first phase, the amalgamation of seven microblocks around 2.5–2.3 Ga formed a stable cratonic block, marking the initial cratonization of the NCC [22,23]. The second phase of cratonization occurred around 2.3–1.82 Ga,

involving continental rifting (2.35–1.95 Ga) and subduction–accretion–collision processes (1.95–1.82 Ga) [24–27]. During 1.95–1.80 Ga, the Huai'an terrane underwent three episodes of metamorphism and deformation, which are represented by crustal thickening, extrusion and exhumation, respectively [28]. These three episodes of metamorphism and deformation in the Huai'an terrane during 1.95–1.80 Ga indicate the NW-SE compressional tectonic regime, marking the final formation of the NCC [29,30]. Previous research about the Huai'an terrane has primarily focused on the tectonic background during the Late Archaean to Early Paleoproterozoic, as well as the metamorphic events and magmatic events during the Late Paleoproterozoic [31–36]. However, there is a lack of in-depth studies on the singularities of magmatic events concerning crustal growth processes during the Middle to Late Paleoproterozoic [37,38].

3.1. Datasets

To understand the magmatic events and tectonic evolution of the Huai'an terrane, 12 granite samples were collected along the Datong–Shangyi fault zone, with nearly equal spacing from north to south of the Huai'an terrane for zircon U-Pb dating (Figure 2). The 129 spots analyzed for zircon U-Pb ages of these 12 granites are listed in Supplementary Table S1. Additionally, 73 granite samples in the TNCO from 26 published papers were incorporated to provide a more comprehensive dataset for zircon U-Pb age analysis. The 1439 spots analyzed for zircon U-Pb ages of these 73 granites are listed in Supplementary Table S2. The combined datasets are used herein to investigate magmatic activity and perform singularity analysis of age peaks, offering valuable insights into the timing and nature of magmatic events and their relationship to tectonic processes in the region.

The combined dataset includes zircon age data from various magmatic events in the TNCO, and their statistical parameters are shown in Table 2. This dataset comprises zircon ages from three distinct magmatic phases, with the age ranges 2.6–2.2 Ga, 2.2–1.9 Ga and 1.9–1.6 Ga. The statistical analysis includes the number of samples, mean age, median age, standard deviation, skewness and kurtosis for each of the three age ranges. These statistics provide insight into the distribution and variability of zircon ages, helping to characterize the magmatic activity in the region.

Table 2. Statistical parameters of granites' magmatic zircon ages from the three phases of magmatic activity in the TNCO.

Age Range (Ga)	2.6–2.2	2.2–1.9	1.9–1.6
Number of Samples	528	530	484
Mean (Ma)	2448.30	2076.51	1812.73
Median (Ma)	2473	2075	1820
Standard Deviation	95.42	68.43	48.43
Skewness	−0.14	−0.12	−0.91
Kurtosis	0.12	0.14	1.25

The granites' zircon magmatic age data are presented in the histogram in Figure 3. The ages of granites in the TNCO mainly fall into three intervals, 2.6–2.2 Ga, 2.2–1.9 Ga, and 1.9–1.7 Ga, with peak values occurring around ~2.53 Ga, ~2.08 Ga, and ~1.84 Ga, respectively. These age distributions highlight key magmatic phases in the region, and the spatial maps in Figure 2 illustrate the geographical extent of these magmatic events.

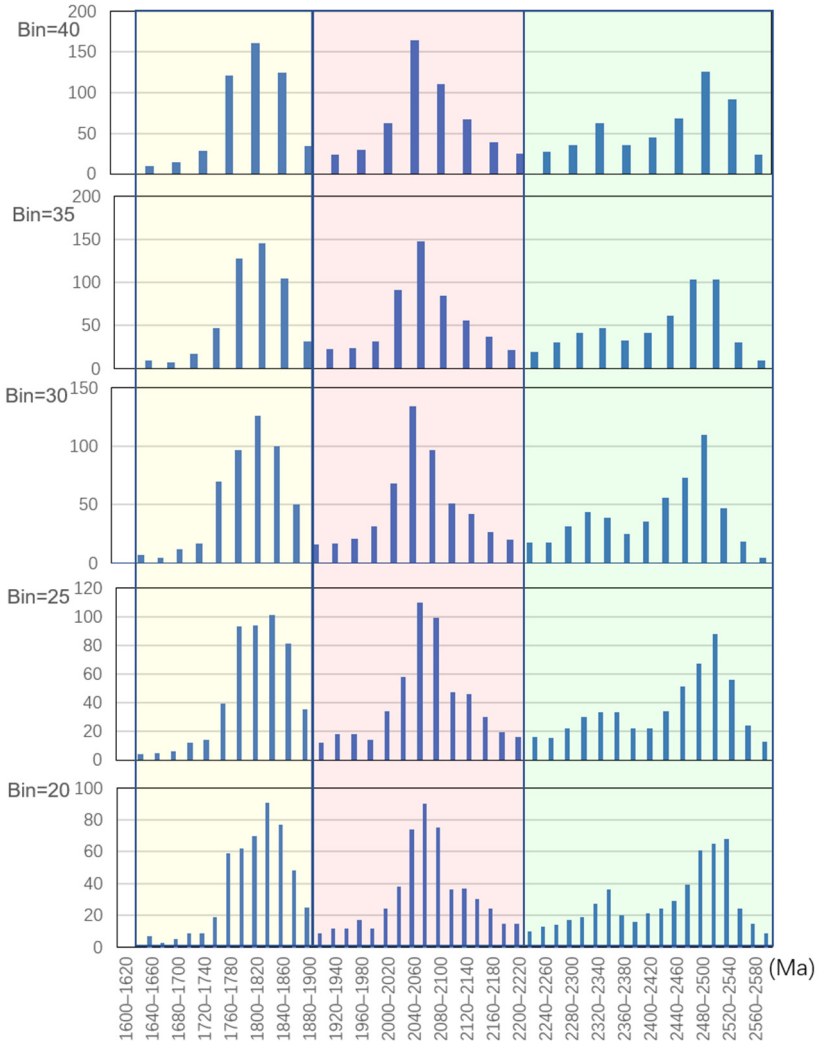

Figure 3. Histograms of granite magmatic zircon age distribution in the TNCO with age bins of 20, 25, 30, 35 and 40 Ma. Color bands present the three ranges with peaks at 2.5, 2.08 and 1.84 Ga.

3.2. Analysis of Magmatic Activity Using Nonlinear Functions

To analyze the variations in magmatic activity, several functions derived in this study in Section 2 were employed, including power-law, logarithmic and exponential functions, each chosen to capture different aspects of nonlinearity and singularity in the data. These functions were applied to quantify the behavior of magmatic activity around the three peaks of the magmatic events.

Statistical analysis was performed using age bins of 20 Ma, 30 Ma and 40 Ma intervals, and the data were converted into time series to represent the probability distribution, minimizing biases due to inconsistent bin sizes. For each time series, a density of the number of age data per unit tie interval around a peak was calculated, and the nonlinear functions derived in this study were applied for analysis. The age density of the time series is calculated as follows:

$$\rho(\Delta t) = \frac{1}{\Delta t} N(\Delta t), \tag{9}$$

where Δt represents the age interval around an age peak, $N(\Delta t)$ is the number of zircon ages within the age range of t $\pm$ 1/2Δt and $\rho(\Delta t)$ represents the average age density [16].

The average age densities for both sides and one side of the three magmatic event peaks were calculated. One of the six types of functions as shown in Table 1 was fitted using the least squares method. The left side of the peak corresponds to younger ages,

while the right side corresponds to older ages. The analysis results for the three peaks are displayed in Figures 4–6.

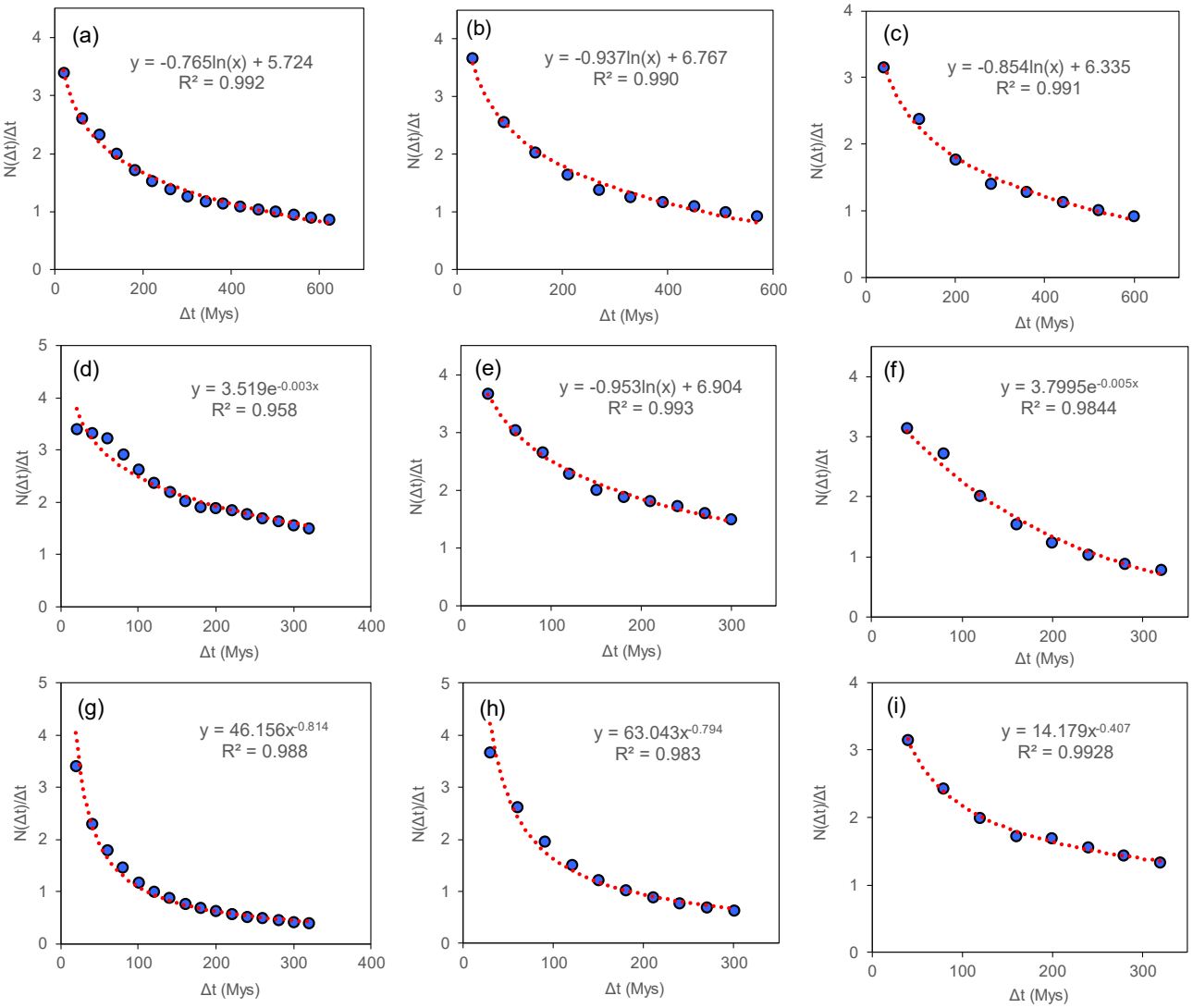

Figure 4. Analysis results of zircon age anomalies of granitic magmatism centered around 2.53 Ga in the TNCO: (**a**,**d**,**g**) the average age density results and function fitting for intervals with a bin size of 20 Ma; (**b**,**e**,**h**) the average age density results for intervals with a bin size of 30 Ma; and (**c**,**f**,**i**) the average age density results for intervals with a bin size of 40 Ma. Each set focuses on both sides of the peak, the left side and the right side of the peak, respectively. Blue dots represent the average age density and dashed red lines for fitted curves according to nonlinear models by LS method.

The results indicate that the trends on both sides of the peaks for the three magmatic episodes are similar. However, the density attenuation curves fitted by the LS method exhibit significant differences in form, particularly showing evident asymmetry around the peaks.

For the magmatic activity during 2.6–2.2 Ga, the average attenuation variations on both sides of the peak (2.53 Ga) can be fitted with logarithmic functions, indicating a logarithmic decrease in anomaly intensity from the center outward. On the right side of the peak (earlier than 2.53 Ga), the density of magmatic activity increases rapidly, following a power-law form, while after the peak, the activity decreases logarithmically. This asymmetry suggests that the magma intrusion rate was fast, while the decline and cessation of magmatic activity were relatively slow. The earlier period (log-log linear) exhibits stronger nonlinearity compared to the later period (log-linear).

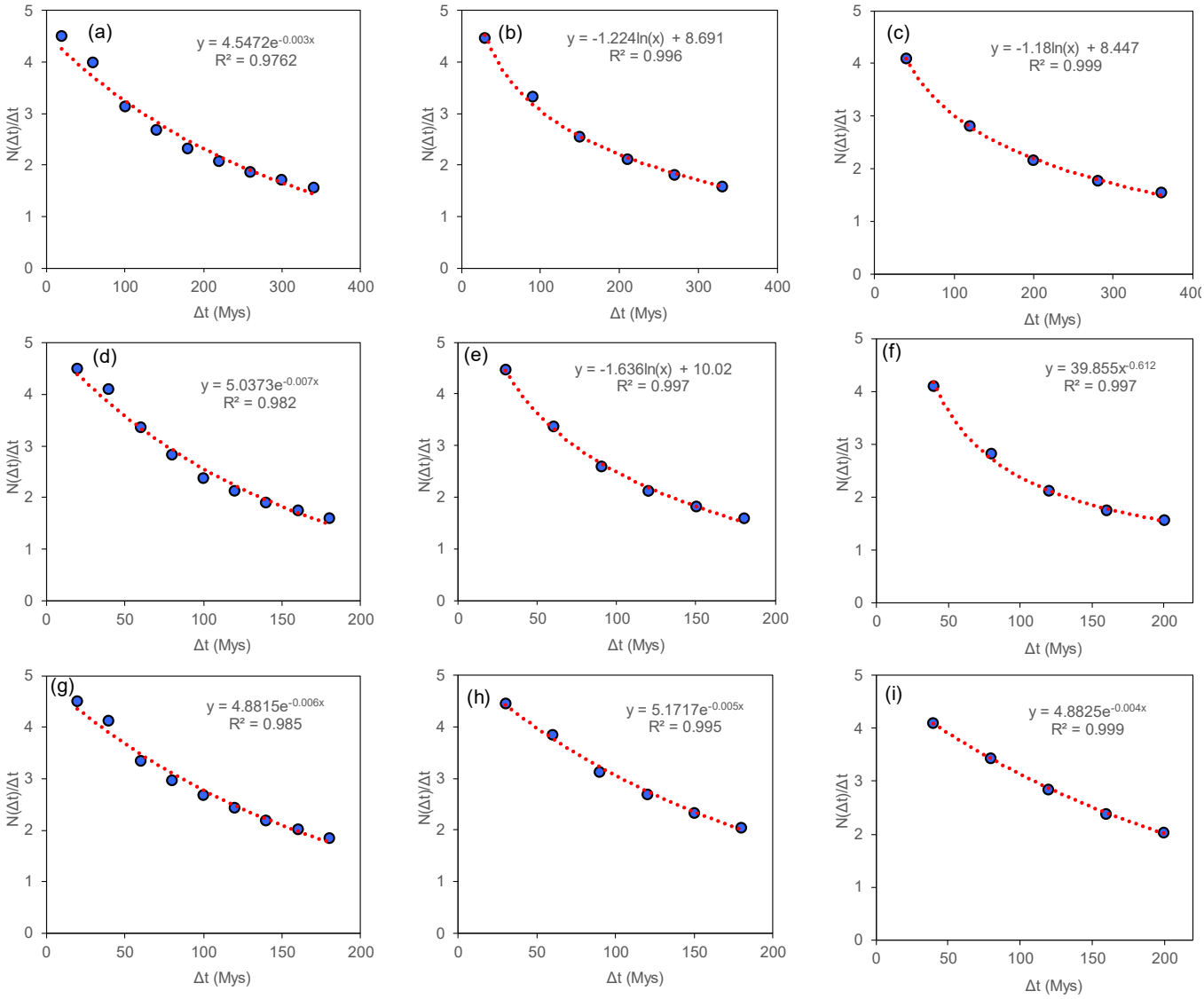

Figure 5. Analysis results of zircon age anomalies of granitic magmatism centered around 2.08 Ga in the TNCO: (**a**,**d**,**g**) the average age density results and function fitting for intervals with a bin size of 20 Ma; (**b**,**e**,**h**) the average age density results for intervals with a bin size of 30 Ma; and (**c**,**f**,**i**) the average age density results for intervals with a bin size of 40 Ma. Each set focuses on both sides of the peak, the left side and the right side of the peak, respectively. Blue dots represent the average age density and dashed red lines for fitted curves according to nonlinear models by LS method.

For the magmatic activity during 2.2–1.9 Ga, the magmatic activity on both sides of the peak (earlier than 2.08 Ga and later) follows either logarithmic or exponential attenuation functions, indicating a less pronounced asymmetry compared to the earlier period.

For the magmatic activity during 1.9–1.6 Ga, the attenuation around the peak (1.84 Ga) and on both sides is characterized by exponential functions with small exponents, reflecting a weaker degree of nonlinearity compared to the earlier two episodes. This final episode no longer exhibits singularity.

The three magmatic episodes exhibit distinct nonlinear and singularity characteristics, with strong linearity and singularity represented by a power-law function fitted to the first peak on the right side, transitioning to a mix of logarithmic and exponential functions in the second peak, and culminating in purely exponential functions at the last peak. These variations likely reflect differences in the deep mechanisms driving the magmatic activity as to be discussed.

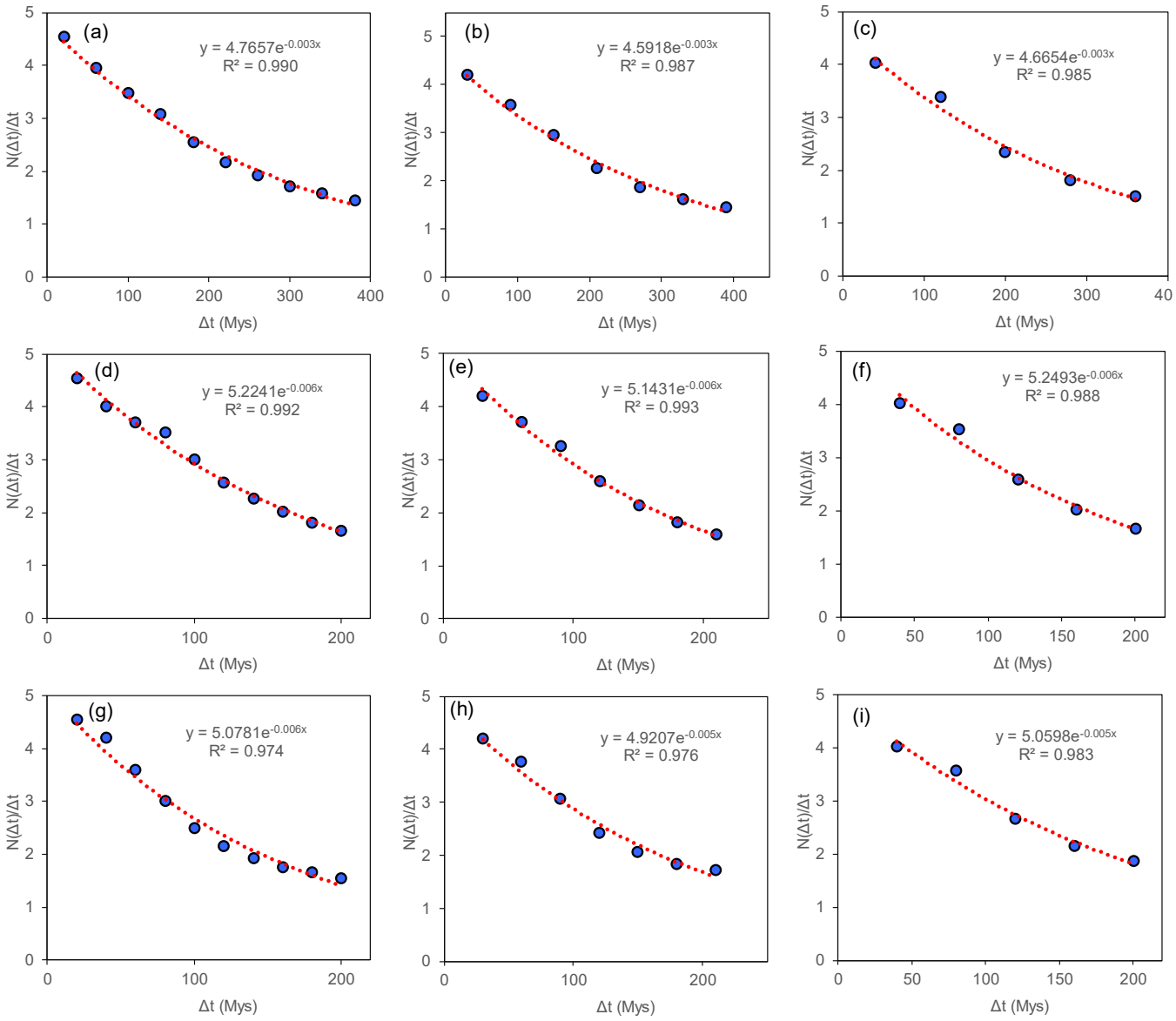

Figure 6. Analysis results of zircon age anomalies of granitic magmatism centered around 1.84 Ga in the TNCO: (**a**,**d**,**g**) the average age density results and function fitting for intervals with a bin size of 20 Ma; (**b**,**e**,**h**) the average age density results for intervals with a bin size of 30 Ma; and (**c**,**f**,**i**) the average age density results for intervals with a bin size of 40 Ma. Each set focuses on both sides of the peak, the left side and the right side of the peak, respectively. Blue dots represent the average age density and dashed red lines for fitted curves according to nonlinear models by LS method.

4. Discussion

4.1. Magmatic Events and Crustal Growth and Reworking

Geochemical and isotopic data of granitoid rocks from the Chengde and Wutai terranes highlight the widespread magmatic activity during 2.6–2.2 Ga [39–41]. Granitic rocks of 2.6–2.54 Ga indicate crustal growth and magmatic processes associated with the assembly of the early continental crust. Specifically, early Proterozoic granitic magmatism is well documented in the TNCO, with zircon εHf(t) values and T_{DM} data suggesting a relatively uniform magma source for 2.2–1.9 Ga granitoids [42]. The presence of A-type and I-type granites in Dengfeng and Hengshan terranes (2.50 Ga and 2.37–2.47 Ga, respectively) points to crustal growth through mantle-derived magmatism. The TNCO during 2.6–2.2 Ga is in a subduction tectonic setting, where the subduction of the oceanic crust beneath the continental crust led to mantle wedge melting and the intrusion of basaltic magma into

the lower crust, further increasing the overall volume of newly generated crust [38,43,44] (Figure 7a). This mantle-driven magmatism is consistent with the evolution of an active continental margin, forming the foundation for the crustal growth of the TNCO during 2.6–2.2 Ga.

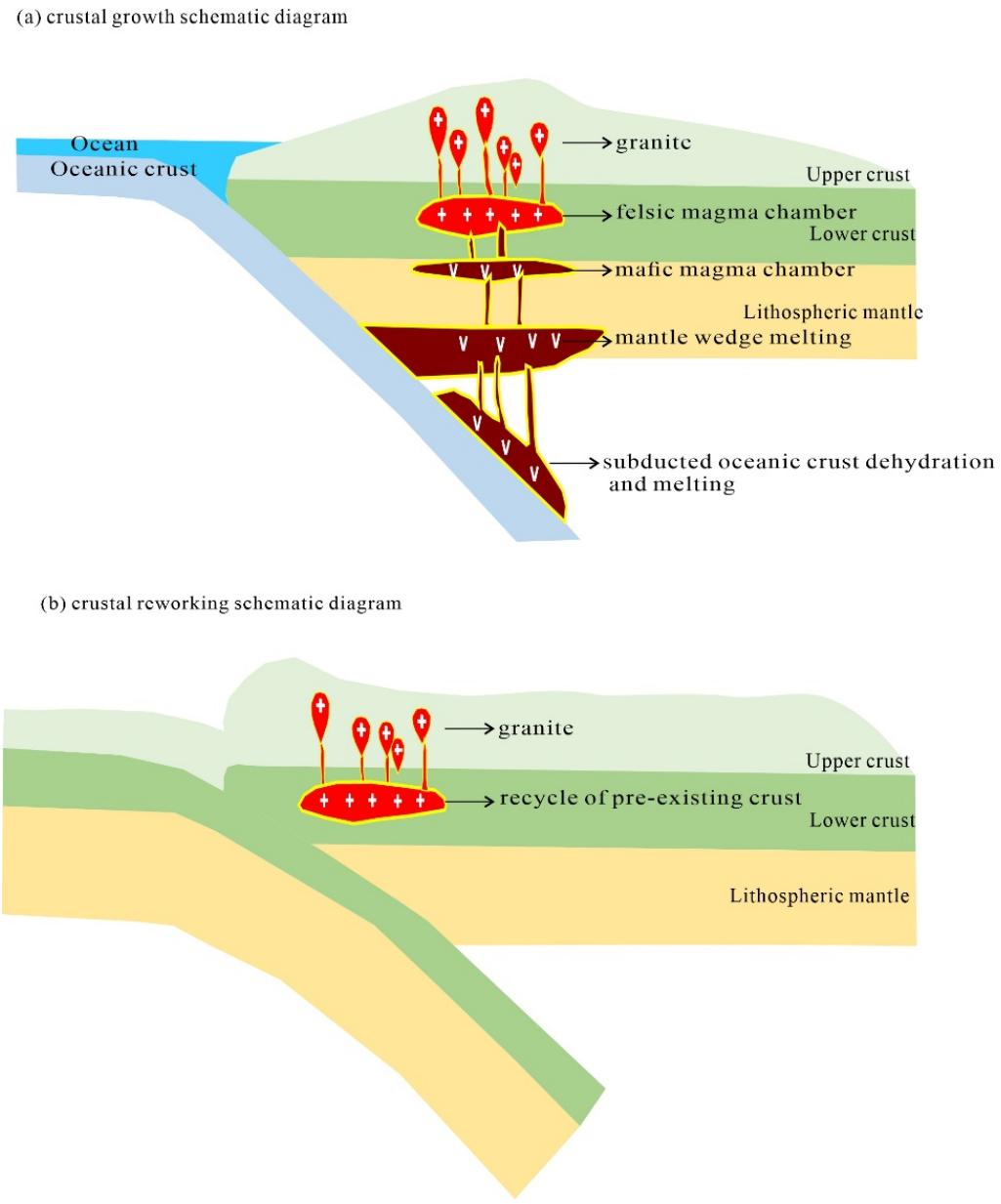

Figure 7. Schematic diagrams illustrating models of crustal growth and crustal reworking.

The geochemical data from various rocks in the TNCO indicate a complex transition from crustal growth to reworking during 2.2–1.9 Ga [35]. In the Hengshan terrane, the 2.05–2.06 Ga granite exhibits negative εHf(t) values, suggesting that the magma primarily derived from the partial melting of the lower crust, indicating crustal reworking [45]. The 2.14 Ga granite from the Wutai terrane displays mixed isotopic signatures, indicating a combination of mantle and lower crustal sources, signifying crustal growth and reworking [46]. In the Fuping terrane, the A-type granites at 2.08–2.07 Ga show positive εHf(t) values, indicating that the magma originated from newly formed, depleted mantle or lower crust, which reflects crustal growth and reworking [47]. These findings suggest that during 2.2–1.9 Ga, the TNCO transitioned from crustal growth to reworking, with

the involvement of mantle-derived and ancient lower crustal materials. This transitional phase was influenced by tectonic activities such as subduction and continental rifting, with notable mantle-derived basaltic and acidic magmatic events marking this era [48,49].

Geological evidence from the terranes of Chengde, Lüliang and Taihua indicates extensive granite magmatism during 1.9–1.7 Ga, pointing to the partial melting of ancient lower crust as the source of these magmas [38,39,50]. The εHf (t) values of zircon grains from the 1.9–1.7 Ga granite magmatism show considerable variability, suggesting complex sources and heterogeneous composition of the underlying crust [51]. Specifically, in the Chengde terrane, the 1.91–1.75 Ga granitic magmatism indicates the reworking of the ancient lower crust, with the εHf (t) values ranging from −6.20 to −1.70 and T_{DM1} values between 2.33 and 2.50 Ga, supporting the idea of crustal remelting [52]. The Lüliang terrane also exhibits evidence of crustal reworking through partial melting of the older lower crust, with magmatic ages ranging from 1.88 to 1.79 Ga [50,53]. The collision between the Eastern and Western blocks of the NCC, which likely occurred along the western margin of the TNCO during 1.9–1.7 G, resulted in crustal reworking by the partial melting of older lower crust (Figure 7b).

4.2. Nonlinearity and Singularity of Magmatic Events

The differences in nonlinearity and singularity across the three magmatic periods (2.6–2.2 Ga, 2.2–1.9 Ga and 1.9–1.6 Ga) can be linked to the evolving tectonic settings and processes driving magmatic activity during each period:

(1) Period 1: 2.6–2.2 Ga (Late Archaean to Early Proterozoic)

The power-law behavior of the density function formed prior to the peak (rapid increase in magmatic activity) suggests a fast, dynamic process, such as the rapid intrusion of magma due to active subduction zones. The transition to logarithmic decay after the peak reflects a gradual cessation of activity, as magmatic processes slowed down. This strong nonlinearity is indicative of a tectonically driven burst of magmatic activity, driven by the rapid convergence and subduction processes. The singularity on the right side of the peak could indicate a highly focused, intense magmatic episode, such as crustal growth via mantle-derived magmatism, with sudden onset and a slow tapering off. During 2.6–2.2 Ga, the strong nonlinearity (power-law function and logarithmic function) and singularity are linked to the dynamic and intense subduction-related magmatism, where rapid mantle-derived intrusion and crustal growth led to quick magma emplacement and slower cessation.

(2) Period 2: 2.2–1.9 Ga (Early Proterozoic)

The less pronounced asymmetry and the shift to logarithmic or exponential attenuation functions indicate a less intense but more stable magmatic environment. The decrease in nonlinearity reflects a tectonic environment where magmatic activity was still driven by subduction or rifting but with a more gradual and less explosive nature. This indicates that tectonic forces had stabilized, and the magma generation was less sudden, with more gradual and prolonged magmatic events. During 2.2–1.9 Ga, the less pronounced asymmetry and more gradual decay (logarithmic/exponential) reflect the transition phase from crustal growth to reworking and complex tectonic interaction (e.g., rifting and arc-continent collision) resulted in less intense but prolonged magmatic activity.

(3) Period 3: 1.9–1.6 Ga (Paleoproterozoic)

The weaker nonlinearity and the shift to purely exponential decay after the peak suggest a much more mature and stabilized tectonic setting. Magmatic processes during this period were likely more uniform and continuous, with fewer sudden peaks in activity. The lack of singularity indicates a more homogeneous magmatic system and the absence of

large, sudden influxes of magma from the mantle. Instead, magma derived from crustal partial melting led to a more gradual, steady decay in magmatic activity. During 1.9–1.6 Ga, the weak nonlinearity and absence of singularity indicate a period of stable tectonics with crustal partial melting. The more uniform and continuous magmatic processes reflect a tectonic environment where continental crusts had stabilized and magmatic activity was much less intense.

In conclusion, these differences between the three magmatic events are tied to the changes in tectonic regimes, where the earlier periods were more dynamic with rapid mantle processes, while later periods reflected the slow, steady evolution of crustal structures.

5. Conclusions

This study highlights the application of nonlinear models—specifically power-law, logarithmic and exponential functions—in understanding the temporal and spatial dynamics of magmatic events, with a particular focus on the Huai'an terrane. Through the analysis of U-Pb zircon dating, Lu-Hf isotopes and geochemical data, the research has shown that these nonlinear models offer valuable insights into the complex tectonic evolution of the NCC, revealing distinct phases of crustal growth and reworking. The power-law function and logarithmic functions effectively capture the intense magmatic activity of 2.6–2.2 Ga, with clear singularity and high nonlinearity. In contrast, the mix of logarithmic and exponential models with small exponents describe the transitional phases (2.2–1.9 Ga and 1.9–1.7 Ga), where magmatic processes evolved more gradually due to changing tectonic conditions, such as subduction and continental rifting.

By applying the nonlinear models, this study provides a new framework for analyzing extreme geological events, emphasizing the nonlinear nature of geological processes. This work may contribute to the broader field of tectonic evolution by demonstrating how nonlinear functions, particularly those exhibiting singularity behaviors, can be used to unravel the intricate dynamics of Earth's magmatic history. It must be remembered that the degree of statistical significance of LS fittings to the data with different functions is relatively small. More high-quality data are needed to validate the findings in the study area or other areas in further study. Given the quality of data and the limited case studies focused on a single area within the NCC, the results may not be broadly generalized to other regions or events. Further studies and validations are required to strengthen this line of research. Nevertheless, the distinctions and similarities among the nonlinear models discussed, as well as their quantification based on nonlinearity and singularity, offer valuable insights. These findings can facilitate the effective utilization and interpretation of these functions in describing anomalies associated with extreme geological events.

Supplementary Materials: The following supporting information can be downloaded at https://www.mdpi.com/article/10.3390/fractalfract9010038/s1, Table S1: Zircon U-Pb LA-ICP-MS data of granites samples from this study; Table S2: Zircon ages of granites from published papers with references [34,38–42,45–48,50–65].

Author Contributions: Conceptualization, methodology, software, formal analysis, interpretation, writing—original draft preparation, writing—review and editing, funding acquisition, Q.C.; investigation, data curation, writing—review and editing, M.G. All authors have read and agreed to the published version of the manuscript.

Funding: This research was jointly funded by the National Natural Science Foundation of China, grant number 42050103, 42430111 and by the Guangdong Province Introduced Innovative R&D Team of Big Data—Mathematical Geosciences and Extreme Geological Events Team (2021ZT09H399).

Data Availability Statement: The data used in the current study can be accessed in the Supplementary Materials.

Acknowledgments: The authors sincerely thank the three anonymous reviewers for their critical review of the paper and their constructive comments, which have significantly enhanced its quality and presentation.

Conflicts of Interest: The authors declare no conflicts of interest.

References

1. Cheng, Q. Long-range effects of mid-ocean ridge dynamics on earthquakes, magmatic activities, and mineralization events in plate subduction zones. *Earth Sci. Front.* **2024**, *31*, 001–014.
2. Cheng, Q. Quantitative simulation and prediction of extreme geological events. *Sci. China Earth Sci.* **2022**, *65*, 1012–1029. [CrossRef]
3. Roman, S.; Bertolotti, F. A master equation for power-laws. *R. Soc. Open Sci.* **2022**, *9*, 220531. [CrossRef]
4. Ma, Z.S. Coupling power-laws offers a powerful modeling approach to certain prediction/estimation problems with quantified uncertainty. *Front. Appl. Math. Stat.* **2022**, *8*, 801830. [CrossRef]
5. Chen, Y. Power-law distributions based on exponential distributions: Latent scaling, spurious Zipf's law, and fractal rabbits. *Fractals* **2015**, *23*, 1550009. [CrossRef]
6. Chu-Shore, J.; Westover, M.B.; Bianchi, M.T. Power-law versus exponential state transition dynamics: Application to sleep-wake architecture. *PLoS ONE* **2010**, *5*, e14204. [CrossRef]
7. Vandewalle, H. Modelling of running performances: Comparisons of power-law, hyperbolic, logarithmic, and exponential models in elite endurance runners. *BioMed Res. Int.* **2018**, *23*, 8203062. [CrossRef]
8. Wymore, A.S.; Larsen, W.; Kincaid, D.W.; Underwood, K.L.; Fazekas, H.M.; McDowell, W.H.; Murray, D.S.; Shogren, A.J.; Speir, S.L.; Webster, A.J. Revisiting the origins of the power-law analysis for the assessment of concentration-discharge relationships. *Water Resour. Res.* **2023**, *59*, e2023WR034910. [CrossRef]
9. Gao, M.; Zhang, Z.; Cheng, Q.; Grujic, D. Zircon U-Pb and Lu-Hf isotopes of Huai'an complex granites, North China Craton: Implications for crustal growth, reworking and tectonic evolution. *Gondwana Res.* **2021**, *90*, 118–134. [CrossRef]
10. Yong, D.H.; Freedman, A.R. *University Physics with Modern Physics*, 13th ed.; Pearson: London, UK, 2012.
11. Kramer, G.H. *Radioactive Decay and the Exponential Law. Nuclear Physics: Principles and Applications*; Wiley: Hoboken, NJ, USA, 1997.
12. Cheng, Q. A combined power-law and exponential model for streamflow recessions. *J. Hydrol.* **2008**, *352*, 157–167. [CrossRef]
13. Cheng, Q. A First-Order Non-Linear Differential Equation Characterizing Multiple Types of Probability Distributions. In *Geostatistical and Geospatial Approaches for the Characterization of Natural Resources in the Environment*; Raju, N., Ed.; Springer: Cham, Switzerland, 2016. [CrossRef]
14. Cheng, Q. Singularity theory and methods for mapping geochemical anomalies caused by buried sources and for predicting undiscovered mineral deposits in covered areas. *J. Geochem. Explor.* **2012**, *122*, 55–70. [CrossRef]
15. Mandelbrot, B.B. *The Fractal Geometry of Nature*; W. H. Freeman and Company: New York, NY, USA, 1982; 216p, ISBN 0-7167-1186-9.
16. Cheng, Q. Singularity analysis of magmatic flare-ups caused by India—Asia collisions. *J. Geochem. Explor.* **2018**, *189*, 25–31. [CrossRef]
17. Cheng, Q. Fractal Derivatives and Singularity Analysis of Frequency—Depth Clusters of Earthquakes along Converging Plate Boundaries. *Fractal Fract.* **2023**, *7*, 721. [CrossRef]
18. Zhao, G.; Sun, M.; Wilde, S.A.; Sanzhong, L. Late Archean to Paleoproterozoic evolution of the North China Craton: Key issues revisited. *Precambrian Res.* **2005**, *136*, 177–202. [CrossRef]
19. Liu, P.; Cai, J.; Li, L. Tectonic setting of the Huai'an region: A review. *J. Geodyn.* **2013**, *60*, 69–83.
20. Li, L.; Zhang, J.; Liu, P. Geology and tectonic history of the North China Craton and its orogenic belts. *Tectonophysics* **2014**, *635*, 24–38.
21. Cai, J.; Li, L.; Zhang, J. Tectonic evolution of the Huai'an region, North China Craton. *J. Geol.* **2015**, *43*, 125–145.
22. Kusky, T.M.; Li, J.; Santosh, M. The Paleoproterozoic North Hebei Orogen: North China craton's collisional suture with the Columbia supercontinent. *Gondwana Res.* **2007**, *12*, 4–28. [CrossRef]
23. Zhai, M. Cratonization and the Ancient North China Continent: A summary and review. *Sci. China Earth Sci.* **2011**, *54*, 1110–1120. [CrossRef]
24. Kusky, T.M.; Li, J.H.; Tucker, R.D. The Archean Dongwanzi ophiolite complex, North China craton: 2.505-Billion-year-old oceanic crust and mantle. *Science* **2001**, *292*, 1142–1145. [CrossRef] [PubMed]
25. Kusky, T.M.; Li, J. Paleoproterozoic tectonic evolution of the North China Craton. *J. Asian Earth Sci.* **2003**, *22*, 383–397. [CrossRef]
26. Zhai, M.; Liu, W. Palaeoproterozoic tectonic history of the North China craton: A review. *Precambrian Res.* **2003**, *122*, 183–199. [CrossRef]

27. Zhai, M. Lower crust and lithospheric mantle beneath the North China Craton before the Mesozoic lithospheric disruption. *Acta Petrol. Sin.* **2008**, *24*, 2185–2204.
28. Zhao, G.; Cawood, P.A.; Wilde, S.A.; Sun, M.; Lu, L. Metamorphism of basement rocks in the Central Zone of the North China Craton: Implications for paleoproterozoic tectonic evolution. *Precambrian Res.* **2000**, *103*, 55–88. [CrossRef]
29. Wu, J.; Zhai, M.; Zhang, H.F.; Guo, J.; Wang, H.; Yang, W.; Zhang, H.; Hu, B. Petrologic indicators of prograde metamorphism in Paleoproterozoic garnet mafic granulites from the Huai'an complex, North China Craton. *Sci. Bull.* **2018**, *63*, 81–84. [CrossRef]
30. Liu, H.; Li, X.P.; Kong, F.M.; Santosh, M.; Wang, H. Ultra-high temperature overprinting of high pressure pelitic granulites in the Huai'an complex, North China Craton: Evidence from thermodynamic modeling and isotope geochronology. *Gondwana Res.* **2019**, *72*, 15–33. [CrossRef]
31. Liu, W.; Zhang, X.; Wu, S. Late Archaean to Early Paleoproterozoic tectonic evolution of the North China Craton: Evidence from the Huaian region. *Earth Planet. Sci. Lett.* **2009**, *284*, 395–410.
32. Wu, F.; Zhang, F.; Li, Y. Late Paleoproterozoic metamorphic events in the Huaian region, North China Craton. *J. Metamorph. Geol.* **2017**, *35*, 487–506.
33. Zhang, J.; Wang, Y.; Liu, P. Paleoproterozoic tectonic evolution and crustal growth of the North China Craton: Insights from the Huaian region. *Geol. Soc. Am. Bull.* **2016**, *128*, 1062–1082.
34. Zhao, G.; Wilde, S.A.; Sun, M.; Guo, J.; Kröner, A.; Li, S.Z.; Li, X.P.; Zhang, J. SHRIMP U-Pb zircon geochronology of the Huai'an Complex: Constraints on Late Archean to Paleoproterozoic magmatic and metamorphic events in the Trans-North China Orogen. *Am. J. Sci.* **2008**, *308*, 270–303. [CrossRef]
35. Gao, M.; Zhang, Z.J.; Cheng, Q.M.; Grujic, D.; Santosh, M. Paleoproterozoic TTG gneisses and granites of the Huai'an Complex: Geochemical and zircon U-Pb-Hf data provide insights into subduction history and crustal growth. *Precambrian Res.* **2022**, *380*, 106823. [CrossRef]
36. Zhang, Z.J.; Kusky, T.; Gao, M.; Cheng, Q.M. Spatio-temporal analysis of big data sets of detrital zircon U-Pb geochronology and Hf isotope data: Tests of tectonic models for the Precambrian evolution of the North China Craton. *Earth-Sci. Rev.* **2023**, *239*, 104372. [CrossRef]
37. Zhang, H.; Liu, Z.; Wang, J. Granitic magmatism in the Huaian region: Geochemistry and tectonic implications. *J. Geol.* **2011**, *119*, 134–148.
38. Wang, G.D.; Wang, H.Y.C.; Chen, H.X.; Zhang, B.; Zhang, Q.; Wu, C.M. Geochronology and geochemistry of the TTG and potassic granite of the Taihua complex, Mts. Huashan: Implications for crustal evolution of the southern North China Craton. *Precambrian Res.* **2017**, *288*, 72–90. [CrossRef]
39. Jiang, N.; Liu, Y.; Zhou, W.; Yang, J.; Zhang, S. Derivation of Mesozoic adakitic magmas from ancient lower crust in the North China craton. *Geochim. Cosmochim. Acta.* **2007**, *71*, 2591–2608. [CrossRef]
40. Miao, L.; Qiu, Y.; McNaughton, N.; Luo, Z.; Groves, D.; Zhai, Y.; Fan, W.; Zhai, M.; Guan, K. SHRIMP U-Pb zircon geochronology of granitoids from Dongping area, Hebei Province, China: Constraints on tectonic evolution and geodynamic setting for gold metallogeny. *Ore Geol. Rev.* **2002**, *19*, 187–204. [CrossRef]
41. Wilde, S.A.; Cawood, P.A.; Wang, K.; Nemchin, A.L. Granitoid evolution in the late Archean Wutai Complex, North China Craton. *J. Asian Earth Sci.* **2005**, *24*, 597–613. [CrossRef]
42. Zhou, Y.Y.; Zhao, T.P.; Wang, C.Y.; Hu, G.H. Geochronology and geochemistry of 2.5 to 2.4 Ga granitic plutons from the southern margin of the North China Craton: Implications for a tectonic transition from arc to post-collisional setting. *Gondwana Res.* **2011**, *20*, 171–183. [CrossRef]
43. Bai, X.; Liu, S.; Guo, R.; Wang, W. Zircon U-Pb-Hf isotopes and geochemistry of two contrasting Neoarchean charnockitic rock series in Eastern Hebei, North China Craton: Implications for petrogenesis and tectonic setting. *Precambrian Res.* **2015**, *267*, 72–93. [CrossRef]
44. Diwu, C.; Sun, Y.; Si, B.; Yan, M. Archean continental crustal growth and reworking of the North China Craton: Constraints from zircon U–Pb age and Hf isotopic composition. *Earth-Sci. Rev.* **2024**, *248*, 104624. [CrossRef]
45. Zhao, R.F.; Guo, J.H.; Peng, P.; Liu, F. 2.1Ga crustal remelting event in Hengshan Complex: Evidence from zircon U-Pb dating and Hf-Nd isotopic study on potassic granites. *Acta Petrol. Sin.* **2011**, *27*, 1607–1623.
46. Du, L.; Yang, C.; Wang, W.; Ren, L.; Wan, Y.; Wu, J.; Zhao, L.; Song, H.; Geng, Y.; Hou, K. Paleoproterozoic rifting of the North China Craton: Geochemical and zircon Hf isotopic evidence from the 2137Ma Huangjinshan A-type granite porphyry in the Wutai area. *J. Asian Earth Sci.* **2013**, *72*, 190–202. [CrossRef]
47. Wang, J.; Yang, C.; Wyman, D.A.; Song, H.; Du, L. Petrogenesis and tectonic implications of the 2.1–2.0 Ga granitoids in Fuping Complex, North China Craton: Constraints from petrology, geochemistry and zircon U-Pb-Hf isotopes. *Precambrian Res.* **2020**, *339*, 105611. [CrossRef]
48. Santosh, M.; Yang, Q.Y.; Teng, X.; Tang, L. Paleoproterozoic crustal growth in the North China Craton: Evidence from the Lüliang Complex. *Precambrian Res.* **2015**, *263*, 197–231. [CrossRef]

49. Yang, C.; Du, L.; Ren, L.D.; Song, H.X.; Wan, Y.S.; Xie, H.Q.; Liu, Z.X. The age and petrogenesis of the Xuting granite in the Zanhuang Complex, Hebei Province: Constraints on the structural evolution of the Trans-North China Orogen, North China Craton. *Acta Petrol. Sin.* **2011**, *27*, 1003–1016.
50. Yu, X.; Liu, J.; Li, C.; Chen, S.; Dai, Y. Zircon U-Pb dating and Hf isotope analysis on the Taihua Complex: Constraints on the formation and evolution of the Trans-North China Orogen. *Precambrian Res.* **2013**, *230*, 31–44. [CrossRef]
51. Zhao, J.; Zhang, C.; Guo, X.; Liu, X. The late-Paleoproterozoic I- and A-type granites in Lüliang Complex, North China Craton: New evidence on post-collisional extension of Trans-North China Orogen. *Precambrian Res.* **2018**, *318*, 70–88. [CrossRef]
52. Zhang, S.H.; Liu, S.W.; Zhao, Y.; Yang, J.H.; Song, B.; Liu, X.M. The 1.75-1.68 Ga anorthosite-mangerite-alkali granitoid-rapakivi granite suite from the northern North China Craton: Magmatism related to a Paleoproterozoic orogen. *Precambrian Res.* **2007**, *155*, 287–312. [CrossRef]
53. Zhao, G.; Wilde, S.A.; Sun, M.; Li, S.; Li, X.; Zhang, J. SHRIMP U-Pb zircon ages of granitoid rocks in the Lüliang Complex: Implications for the accretion and evolution of the Trans-North China Orogen. *Precambrian Res.* **2008**, *160*, 213–226. [CrossRef]
54. Santosh, M.; Liu, D.; Shi, Y.; Liu, S.J. Paleoproterozoic accretionary orogenesis in the North China Craton: A SHRIMP zircon study. *Precambrian Res.* **2013**, *227*, 29–54. [CrossRef]
55. Wang, H.Z.; Zhang, H.F.; Zhai, M.G.; Oliveira, E.P.; Ni, Z.Y.; Zhao, L.; Wu, J.L.; Cui, X.H. Granulite facies metamorphism and crust melting in the Huai'an terrane at ∼1.95 Ga, North China Craton: New constraints from geology, zircon U–Pb, Lu–Hf isotope and metamorphic conditions of granulites. *Precambrian Res.* **2016**, *286*, 126–151. [CrossRef]
56. Zhang, H.F.; Zhai, M.G.; Santosh, M.; Diwu, C.R.; Li, S.R. Geochronology and petrogenesis of Neoarchean potassic meta-granites from Huai'an Complex: Implications for the evolution of the North China Craton. *Gondwana Res.* **2011**, *20*, 82–105. [CrossRef]
57. Zhang, H.F.; Zhai, M.G.; Santosh, M.; Li, S.R. Low-Al and high-Al trondhjemites in the Huai'an Complex, North China Craton: Geochemistry, zircon U-Pb and Hf isotopes, and implications for Neoarchean crustal growth and remelting. *J. Asian Earth Sci.* **2012**, *49*, 203–213. [CrossRef]
58. Fan, W.; Jiang, N.; Zhai, M.; Hu, J. Zircon constraints on granite derivation in the northern North China Craton. *Lithos* **2020**, 356–357. [CrossRef]
59. Kröner, A.; Wilde, S.A.; Brien, P.J.O.; Li, J. Field relationships, geochemistry, zircon ages and evolution of a late Archaean to Palaeoproterozoic lower crustal section in the Hengshan Terrain of northern China. *Acta Geol. Sin.-Engl. Ed.* **2005**, *79*, 605.
60. Tang, L.; Santosh, M.; Teng, X.M. Paleoproterozoic (ca. 2.1-2.0 Ga) arc magmatism in the Fuping Complex: Implications for the tectonic evolution of the Trans-North China Orogen. *Precambrian Res.* **2015**, *268*, 16–32. [CrossRef]
61. Wang, J.; Kusky, T.; Wang, L.; Polat, A.; Deng, H. A Neoarchean subduction polarity reversal event in the North China Craton. *Lithos* **2015**, *220–223*, 133–146. [CrossRef]
62. Du, L.; Yang, C.; Wyman, D.A.; Nutman, A.P.; Lu, Z.; Song, H.; Xie, H.; Wan, Y.; Zhao, L.; Geng, Y.; et al. 2090-2070 Ma A-type granitoids in Zanhuang Complex: Further evidence on a Paleoproterozoic rift-related tectonic regime in the Trans-North China Orogen. *Lithos* **2016**, *254–255*, 18–35. [CrossRef]
63. Wang, J.; Kusky, T.; Polat, A.; Wang, L.; Deng, H.; Wang, S. A late Archean tectonic mélange in the Central Orogenic Belt, North China Craton. *Tectonophysics* **2013**, *608*, 929–946. [CrossRef]
64. Zhao, Y.; Li, N.; Jiang, Y.; Niu, H. Petrogenesis of the Late Archean (∼2.5 Ga) Na- and K-rich granitoids in the Zhongtiao-Wangwu region and its tectonic significance for the crustal evolution of the North China Craton. *Precambrian Res.* **2017**, *303*, 590–603. [CrossRef]
65. Deng, H.; Kusky, T.; Polat, A.; Wang, C.; Wang, L.; Li, Y.; Wang, J. A 2.5 Ga fore-arc subduction-accretion complex in the Dengfeng Granite-Greenstone Belt, Southern North China Craton. *Precambrian Res.* **2016**, *275*, 241–264. [CrossRef]